Computer assisted reconstruction of complex proximal humerus fractures for preoperative planning

Philipp Fürnstahl [a,*], Gábor Székely [a], Christian Gerber [b], Jürg Hodler [b], Jess Gerrit Snedeker [b], Matthias Harders [a]

[a] Computer Vision Laboratory, ETH Zurich, Zurich, Switzerland
[b] Shoulder and Elbow Surgery Group, University Hospital Balgrist, Zurich, Switzerland

ARTICLE INFO

ABSTRACT

Operative treatment of displaced fractures of the proximal humerus is among the most difficult problems in orthopedic shoulder surgery. An accurate preoperative assessment of fragment displacement is crucial for a successful joint restoration. We present a computer assisted approach to precisely quantify these displacements. The bone is virtually reconstructed by multi-fragment alignment. In case of largely displaced pieces, a reconstruction template based on the contralateral humerus is incorporated in the algorithm to determine the optimal assembly. Cadaver experiments were carried out to evaluate our approach. All cases could be successfully reconstructed with little user interaction, and only requiring a few minutes of processing time. On average, the reassembled bone geometries resulted in a translational displacement error of 1.3 ± 0.4 mm and a rotational error of $3.4 \pm 2.2°$, respectively.

1. Introduction

Proximal humerus fractures are the second-most prevalent fractures of the upper arm and account for about 5% of all fractures (Reineck et al., 2007). About 20% of them are considerably displaced, necessitating a treatment by operative reduction (Gerber et al., 2004) or arthroplasty (Kontakis et al., 2008). Bone reconstruction by open reduction with internal fixation is a treatment option for fractures with up to four fragments (Wijgman et al., 2002). Such cases are generally caused by high energy trauma in the young as well as low energy trauma in the elderly, frequently resulting from a fall. The management of these complex fractures is one of the most challenging shoulder problems in orthopedic surgery. An accurate preoperative analysis of the fracture pattern and displacement is critical for the outcome of this intervention (Naranja and Iannotti, 2000).

Computer assisted surgery (CAS) has the potential to facilitate this difficult planning task. Computer-based methods have successfully been used pre- and intra-operatively in various orthopedic areas, such as knee, spine, pelvis or femur surgery (Jaramaz et al., 2006). However, such techniques have only seen limited application for planning of surgical reduction in proximal humerus fractures. In current clinical practice, the planning is based on the examination of 2-d radiographs or 3-d computed tomography (CT) scans. Fractures are classified based on the assessment of fracture

patterns and the degree of displacement. Several classification schemes exist – the one reported by Neer (1970, 2002) being one of the most common.

The exact measurement of displacements is of paramount importance for precise joint restoration, since the original anatomical relationships have to be reproduced as closely as possible. As reported in Shrader et al. (2005), the manual assessment whether a fragment is significantly displaced (by more than 1 cm or 45°) is very difficult. Exact quantification of fragment displacement is extremely challenging and hardly possible by simple visual inspection of radiographs or CT images.

In this paper we present a computer-based system for reduction planning of complex proximal humerus fractures. The technique requires little user interaction, resulting in short planning times. Our main target is to improve current clinical procedures which may be time-consuming and error-prone, as they rely on manual measurements.

The proposed system performs reconstruction based on the registration of the surfaces of neighboring fracture edges (in the following called fracture surfaces). The method combines robust correlation-based matching with multi-piece alignment. Due to the often significant dislocation of fragments in the considered complex fracture, it is not possible to base the registration on the initial fragment positions. Instead, our method relies on automatically finding a sufficiently good estimate for initialization, using the contralateral, healthy bone geometry as a template. To perform this complex planning task in a reasonable time, most parts of the algorithm are designed to run on a graphics processing unit (GPU).

* Corresponding author. Tel.: +41 44 632 5283.
E-mail address: fuernstahl@vision.ee.ethz.ch (P. Fürnstahl).

This allows efficient planning where measurements of fragment displacement can be carried out in approximately 10–20 min.

In the following we will first give an overview of existing related CAS fracture reduction systems. Thereafter, the overall computer-based planning process is outlined in Section 3. The details of our approach are explained in Section 4. The method is verified via cadaver experiments and tested on clinical data, as described in Section 5. A discussion of the work is provided in Section 6, followed by a conclusion in Section 7.

2. Related work

So far only a small number of related systems have been developed. A computer assisted method, dealing with complex proximal humerus fractures, was described by Bicknell et al. (2007). They report on an experimental study for the treatment of 4-part fractures via a hemiarthroplasty. A CAS approach for the placement of the hemiarthroplasty and the reduction of the tuberosity fragments is compared to the traditional surgical technique. The reconstruction was based on manual measurements of seven anatomical characteristics of the bone. Fiducial markers, implemented before CT acquisition, were used for registration of the CT measurements with the actual humerus during surgery. The evaluation was done on seven pairs of cadaveric shoulders according to the derived anatomical measures. While the CAS method seemed promising, it improved accuracy only for one of the seven characteristics. The authors argued that the small number of specimens could be one of the reasons of the low statistical power of the study. The main limitation of their technique appeared to be the simplified fracture model based on the anatomical landmarks, which required four large fragments with easily recognizable patterns.

Another closely related work focuses on planning of fracture reduction of broken femur heads (Okada et al., 2009). Three different methods were proposed based on iterative closest point registration (ICP). Fragments were registered either to the contralateral bone, to fracture surfaces, or to fracture surfaces using the contralateral bone as a constraint. The authors indicate that the first technique, i.e. the contralateral registration, did not lead to satisfactory results due to wrong local minima after poor initialization. The other two registration methods were proposed to overcome these problems. For ICP registration of fracture surfaces, the regions of interest being target for registration were manually defined by the user. Thereafter, the surfaces were sequentially registered in a pre-defined order to the set of already registered pieces. A comparison to our method will be provided in Section 6.

Moghari and Abolmaesumi (2008) proposed an automatic and efficient method for global registration of multiple bone fragments. Similar to our approach, the algorithm comprised local and global registration steps. In the local step, each fragment was initially aligned to an anatomical atlas of the bone based on a statistical model. To this end, a local point descriptor was introduced to identify potential corresponding points between the fragment and the mean shape. The descriptor was based on a normalized quadratic function which was fitted to the local surface patch around each point of interest. For each candidate pair, a similarity transform was applied to match the fragment with the template. To this end the point clouds of the corresponding parts were centered and oriented according to their eigenvectors and eigenvalues. The best fit for each fragment was determined by the similarity transformation yielding the smallest alignment error. After local registration, simultaneous global alignment using Kalman filtering was performed to accurately register all the fragments to each other and to the template. The proposed global alignment method demonstrated high accuracy in a cadaver study.

Although we did not explicitly test the coarse alignment method of Moghari and Abolmaesumi (2008), we had performed experiments with different local point descriptors (Johnson and Hebert, 1999; Douros and Buxton, 2002). However, these descriptors led to a high number of potential matches in case of smaller fragments originating from the humeral head. More importantly, the coarse alignment of the corresponding regions, e.g. by a similarity transform, was not sufficiently accurate to identify the correct fragment position in some of these cases. Therefore, we propose to apply accurate surface registration already in the coarse alignment step.

Papaioannou and Karabassi (2003) presented a solution to the assemblage of solid broken artefacts. As a preprocessing step, a region growing algorithm was applied to segment each fragment into planar regions of similar orientation (i.e. fracture facets). Thereafter, all possible combinations of fracture facets were aligned in a pairwise fashion using a surface matching algorithm. Efficient matching was achieved by aligning the facets with respect to their depth maps. Additionally, facet boundary curve matching in conjunction with intersection tests were incorporated in order to reduce the search space. In the last step, the best assembly was obtained by determining the set of fragment combination that resulted in the smallest accumulative matching error. The method's main disadvantage is the requirement of nearly planar fracture facets. This limits the application in the alignment of cortical bone pieces which can be strongly curved.

Apart from these projects a considerable number of methods for fracture reduction planning of long bones exist; some of these being part of comprehensive navigation and robot assisted surgery systems. Westphal et al. (2009) presented a tele-manipulated fracture reduction system for the femur shaft. In case of complex fractures two reduction methods can be applied (Winkelbach et al., 2003, 2004). The method of Winkelbach et al. (2003) was designed to manage the assembly of cylindrical fragments. The cylindrical shape of the pieces is used to calculate their main axes and to match the fracture surfaces. Winkelbach et al. (2004) extended this method for automatic assembly of arbitrarily shaped fragments. An efficient RANSAC approach was proposed where point pairs are randomly selected to estimate the pose and evaluate the matching quality. The algorithm was repeated until a sufficiently good match was achieved. The method was evaluated for several objects including a femur and pelvis bone. Additional constraints have to be used in case of large smooth areas with similar regions on the counterpart. However, the definition of constraints by the user usually implies to have some prior knowledge about the relationship between fragments, e.g. the identification of corresponding fracture surfaces or the correct order in which fragments must be aligned. In complex fractures, the definition of such user-defined correspondences can be very difficult.

Willis et al. (2007) proposed a reconstruction technique for highly fragmented long bones. In contrast to our approach, the segmented spongy bone was included in the assembly. A multi-body ICP algorithm with a modified error metric including CT image intensities was proposed to match the fragments. The method relied on manual identification of likely corresponding fracture surfaces and was tested for a single case of a fractured tibia without accuracy evaluation. Several aspects of the method of Willis et al. were improved by Zhou et al. (2009). The manually defined corresponding surfaces were organized into groups representing the same fragment pair in order to prevent oscillations in the pairwise registration. Additionally, geometrically stable subsampling was incorporated in the pairwise and multi-body alignment steps to improve the registration of featureless surfaces. The performance of the algorithm was demonstrated on one clinical tibial pilon case acquired from CT, as well as on several artificially generated fractures based on bone replicas.

Ron et al. (2003) obtained the periaxial rotation of two-part femur shaft fractures from the contralateral side. The technique was used for intra-operative femur reduction in a CAS system called FRACAS (Joskowicz et al., 1999). Nakajima et al. (2004) used image based registration to align femur fragments to the healthy, mirrored bone. A method for two-part fractures was described, where the volumes of interest of the fragments to be registered were manually defined. After registration, the bone reconstruction was guided intraoperatively by tracking both fragments.

3. Overview of the system

Our overall planning framework is designed in a modular fashion as illustrated in Fig. 1. Dashed rectangles indicate modules which are based on previous work reported by Harders et al. (2007). The data flow through the different modules is represented by lines in Fig. 1.

The input data for the first module, the segmentation part, are CT scans of a patient's fractured humerus head and the mirrored contralateral bone. As a preprocessing step, a bone enhancement filter is applied which relies on a multi-scale sheetness measure (Descoteaux et al., 2006). The sheetness measure is high for voxels of the cortical bone but low for image parts representing other tissue. Therefore, the cortical bone layer is enhanced against its surrounding. The only data-dependent parameter of the filter is the noise suppression value which was set between 60 and 150. After bone enhancement, 3-d region growing is performed on the sheetness image to extract the cortical bone pieces as described in Harders et al. (2007). In most cases, a tolerant region growing threshold is required to accurately segment weak bone boundaries. This typically results in leakage into adjacent pieces due to narrow inter-bone spacing, which has been tolerated in order to keep the manual effort of the segmentation task as low as possible. Connected fragments are separated in a subsequent step.

We propose a semi-automatic method for performing this task. The algorithm relies on the manual identification of fragments. To this end, connected fragments are identified by user-defined seed points. The position of a seed point indicates the component's part which should definitely belong to a certain fragment. Once the seed points are defined, the separation can be computed by performing energy minimization using multi-label graph cut optimization. Basically, the energy function to be minimized consists of a regional and a boundary term as defined in Kolmogorov and Zabih (2004). In our method, the regional term is only used to define hard constraints for voxels which definitely belong to a certain fragment. These hard constraints are set for all voxels in a neighborhood of 5 mm around each seed point. The actual separation of minimal energy is determined by the boundary term

$$V(v, w) = (\bar{S}(v) + \bar{S}(w)) \tag{1}$$

where $\bar{S}(v)$ and $\bar{S}(w)$ are the normalized sheetness values (Harders et al., 2007) of adjacent voxels v and w, respectively. In general, the sheetness value is high at the center of the cortical structure (Descoteaux et al., 2006) and falls off at the bone boundaries. Therefore, Eq. (1) favors cuts between neighboring voxels of low sheetness value.

Thereafter, triangular meshes of the cortical pieces as well as of the contralateral humerus are generated using the Marching Cube algorithm (Lorensen and Cline, 1987). In case of the tested clinical data, a fragment's mesh consists of 84,600 triangles on average. The average mesh size of the contralateral bone is 305,000 triangles. The overall segmentation and separation process can be carried out in a few minutes.

The bone reconstruction modules take the generated triangular meshes as input. Our approach consists of two registration steps. First, the overall best assembly with respect to the mirrored contralateral bone, acting as a reconstruction template, is determined. Bone reconstruction based on the contralateral mesh is described in Section 4.1. The resulting assembly is, however, not optimal due to possible anatomical differences between contralateral sides. Therefore, this assembly is only used as a good initialization for the second stage of our algorithm presented in Section 4.2, performing the final reconstruction based on the registration of fracture surfaces.

Finally, it should be noted that if no contralateral bone is available, the reconstruction could be carried out using the interactive planning environment described by Harders et al. (2007). The sys-
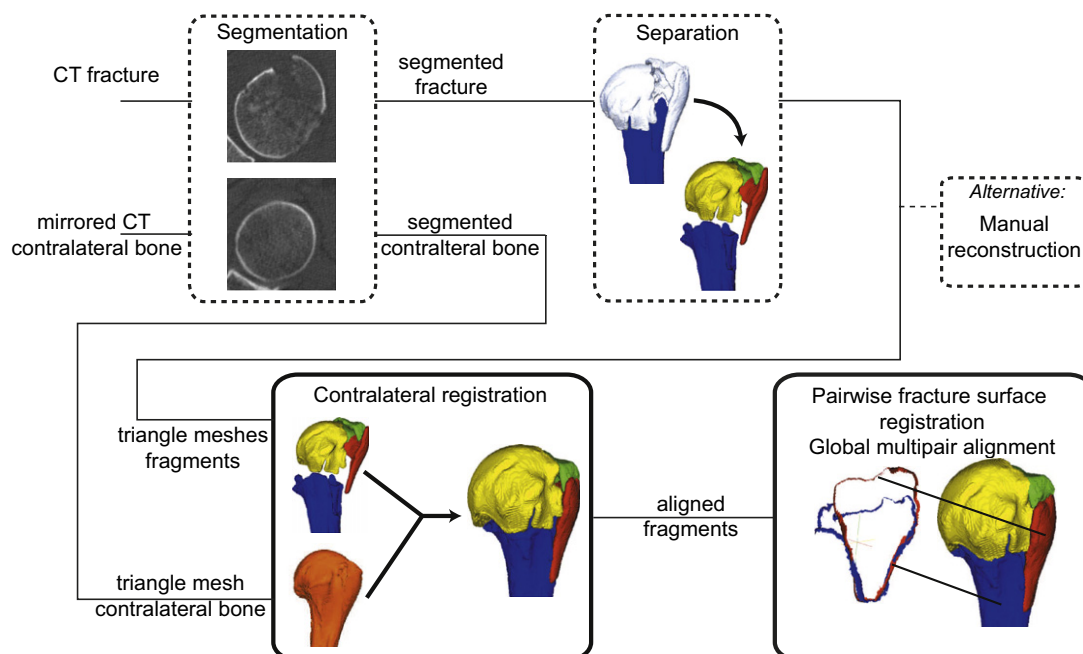

Fig. 1. Overview of the planning framework. Dashed rectangles denote previous work.

tem supports the user by providing haptic feedback, collision detection, and stereo rendering. However, manual assembly may take up to 30 min due the overall complexity of the task.

4. Methodology

4.1. Contralateral matching

The main goal of this registration step is to find a rigid transformation for each fragment in order to reassemble the fracture based on the contralateral geometry. To this end, multiple registrations based on initially coarse alignments with the template are performed for each fragment. The generation of different initial alignments is required to avoid problems with local minima, possibly causing a fragment to converge to an incorrect position. Local minima can occur frequently in the case of the humerus head due to its almost spherical shape. The generation of the transformations representing the initial alignments is described in Section 4.1.1. Thereafter, each fragment is locally registered to the template for each of these alignments and good potential matches are retained. The best assembly is finally obtained by evaluating an error measure that incorporates alignment and overlap errors between all fragments. Algorithmic details of the local registration and final alignment are explained in Section 4.1.2.

4.1.1. Coarse initial alignments on the contralateral bone

In this step a set of initial transformations is generated specifically for each fragment. Each transformation of this set is used to align the fragment with the opposed humerus for later local registration. The number of potential transformations should be small in order to ensure computational efficiency while the contralateral bone has to be covered densely enough to find all potential matches. The transformations are generated by aligning the fragment with candidate points lying on the contralateral bone surface. In the following we describe the required steps to extract candidate points and to calculate the set of transformations for each fragment.

4.1.1.1. Preprocessing. Three preprocessing steps are required to determine the candidate points on the contralateral surface.

1. *Inner surface removal.* Firstly, mesh vertices belonging to the inner contralateral bone surface are excluded from candidate

point generation. Inner and outer surface points can be distinguished based on the local normal vectors, pointing away from the bone on the outer, and to the inside on the inner surface. A ray is cast from each surface mesh point x_i in its normal direction $\mathbf{n}_i$ as shown in Fig. 2a. In case of an outer surface point x_1, the ray does not intersect the mesh while the ray of an inner surface point x_2 crosses the opposed surface. To avoid problems in case of concavities, the ray's origin is offset by Δt. Δt can be chosen conservatively large, but such that the point $x_2 + \Delta t$ is still within the interior of the bone. For instance, the offset can be set to $\Delta t = 1$ cm, being smaller than the minimal cross-sectional diameter of the humerus in the region of interest. After all outer surface points are identified, a connected component analysis is performed and the largest connected region is chosen in order to remove possible erroneous assignments.

2. *Diaphysis registration and removal.* In this step the largest shaft part F_0 of the fracture is selected by the user and registered to the contralateral bone. The resulting transformation will act as the base coordinate system for the reconstruction and all displacements will be represented relative to it. In case of F_0 a rough translational alignment with the contralateral bone is sufficient to find the correct final position by registration, assuming both humeri were acquired in the anatomic position. For automatic alignment, F_0 and the contralateral mesh are centered in the sagittal and coronal plane. The meshes are distally aligned in the axial direction. Thereafter, ICP registration is performed to accurately superimpose both diaphyses. Since this step already determines the correct location of F_0, candidate points for the alignment of the remaining fragments are not required to lie on this part of the contralateral bone. The corresponding contralateral mesh points are excluded from candidate generation by removing all points being in close proximity to F_0. We used a distance threshold of 0.5 mm and a KD-tree (Mount and Arya, 1997) for efficient closest-point queries.

3. *Mesh Simplification.* The size of the remaining contralateral mesh has to be reduced to an acceptable amount in order to use its points as candidates. As a consequence, the mesh must be drastically simplified from hundred-thousands of points to less than hundred, while preserving its basic shape in order to generate good candidates. For this task an efficient simplification algorithm by Lindstrom (2000) was chosen, available in the Visualization Toolkit (Schroeder and Martin, 2004). Based
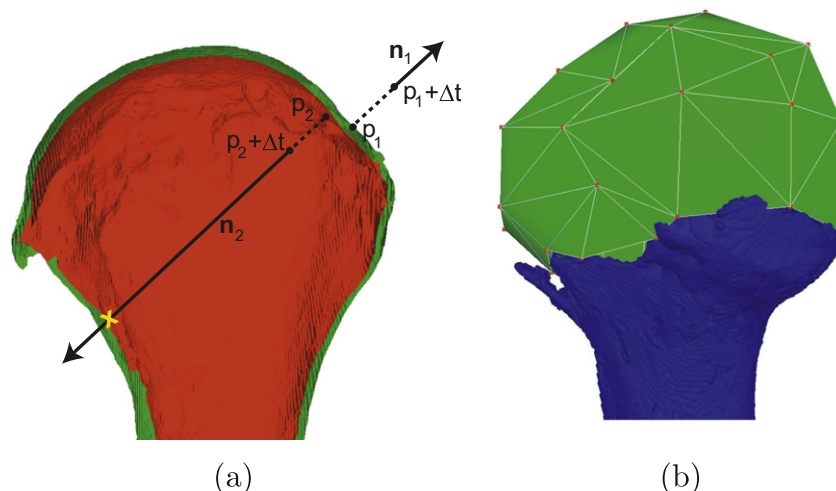

(a)   (b)

Fig. 2. Generation of candidate points. (a) The inner surface (red) is identified and removed using a ray casting technique. Half of the bone was clipped for visualization of the inner surface. (b) Candidate points (red) are determined based on a low resolution representation of the humeral head (green). The blue region belongs to the registered shaft fragment F_0. (For interpretation of the references to colour in this figure legend, the reader is referred to the web version of this article.)

on an appropriate quality setting, the algorithm yielded good visual results with a simplified mesh consisting of points constrained to lie on the original mesh surface. The quality of the simplified mesh is defined by the resolution res_{cand} of a uniform grid. The general approach is to hash the triangle vertices into the grid cells. For each cell an error quadric is calculated that is based on all triangles covered by this cell. Thereafter, a representative vertex per cell is computed using the corresponding quadric. This determines the spatial location of the vertices in the final simplified mesh.

4.1.1.2. Candidate point generation. Good candidate points can be obtained from the surface points of the preprocessed contralateral mesh. However, smaller fragments require a denser set of initializations and thus more candidate points. To this end, we propose to adapt the simplification quality according to the fragment size. The resolution res_{cand} in x, y and z direction of the coordinate system is determined by a step function

$$\#cells(A) = \begin{cases} 2, & A > 6000 \\ 4, & 3000 \leqslant A \leqslant 6000 \\ 5, & A < 3000 \end{cases} \quad (2)$$

where A is the sum of the mesh triangles' area in mm^2, obtained from Heron's formula. Fragments where A is smaller than 3000 mm^2 are typically part of the tuberosity or pieces of a 4-part fracture while the range of 3000–6000 mm^2 considers cases where the head is split in two parts. The remaining case is used for one large head fragment. The thresholds were determined experimentally according to our clinical data. An example of a simplified surface using a resolution of four cells per coordinate direction is shown in Fig. 2b.

4.1.1.3. Transformations. The processing time of the previously described steps is typically less than 30 s and approximately 8–70 candidate points are created per fragment depending on its size. The number of candidates for fragment F_i is denoted by NC_{F_i}. Based on the candidate points $q_{i,j}$, the final set of transformations is calculated for F_i as follows.

An initial translation alignment to the candidate point is obtained by moving the fragment's center c_{F_i} to $q_{i,j}$. The translation is represented by transformation $T_{i,j}^1$ as depicted in Fig. 3a. For the rotational alignment the typical fragment shape is taken into account where a good estimate can be found by aligning the fragment's smallest 2nd moment e_3 with the candidate point's surface

normal $\mathbf{n}_{q_{i,j}}$. Vector $\mathbf{e}_3$ is calculated by an eigenvector analysis of the 3×3 covariance matrix of the coordinates of the fragment's points. The sign of $\mathbf{e}_3$ is automatically determined by a sphere fitting approach, since a correctly aligned fragment typically bends towards the bone center. To this end, two spheres are initialized on each side of the fragment as illustrated in Fig. 4. Both radii are initially set to the radius of the fragment's bounding sphere. The spheres are then iteratively fit to the fragment's points by a least-squares minimization (Schneider and Eberly, 2002). The correct orientation of $\mathbf{e}_3$ is finally determined by defining its sign such that the vector points away from the center of the sphere with the smaller fitting error. The alignment after transformation $T_{i_j}^2$ might still be a suboptimal initial guess for the local matching algorithm since the correct fragment orientation around the aligned axis $\mathbf{e}_3$ is completely unknown. Therefore, the rotation around $\mathbf{e}_3$ is sampled in $\pi/2$ steps denoted by transformations $T_{i,j}^3, T_{i,j}^4$, and $T_{i,j}^5$ in Fig. 3b. In the end, for each fragment and each candidate point four test transformations $\left(T_{i,j}^2 \circ T_{i,j}^1\right), \left(T_{i,j}^3 \circ T_{i,j}^2 \circ T_{i,j}^1\right), \left(T_{i,j}^4 \circ T_{i,j}^2 \circ T_{i,j}^1\right)$, and $\left(T_{i,j}^5 \circ T_{i,j}^2 \circ T_{i,j}^1\right)$ are generated.

4.1.2. Contralateral registration and assembly

In order to identify the best matches, $4 \cdot NC_{F_i}$ initial transformation are iteratively refined by optimizing the fit to the contralateral template for each F_i. It is important to note that the registration template is represented by the initial contralateral mesh and not by the simplified model used in Section 4.1.1.
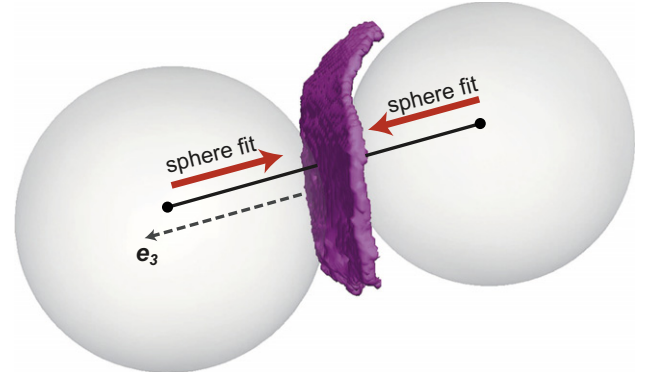

Fig. 4. Determination of the correct orientation of vector $\mathbf{e}_3$. After fitting two spheres to the fragment, $\mathbf{e}_3$ has to point away from the center of the sphere with the smaller error (right sphere).
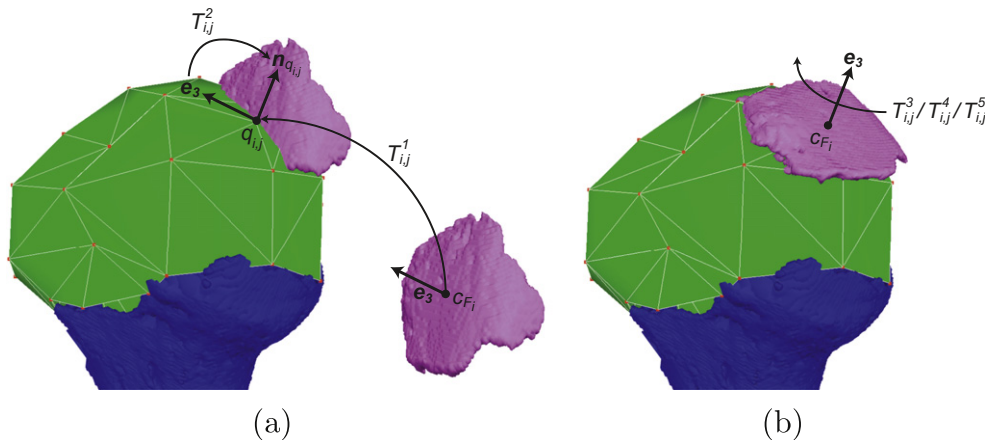

(a)   (b)

Fig. 3. Coarse alignment of a fragment to a candidate point $q_{i,j}$. Four transformations are calculated for each $q_{i,j}$. (a) The fragment's center is translated to $q_{i,j}$ and the fragment's 2nd moment e_3 is aligned with the surface normal $\mathbf{n}_{q_{i,j}}$ at $q_{i,j}$. (b) Three additional transformations are calculated by sampling the rotation around $\mathbf{e}_3$ in $\pi/2$ steps.

For the registration task, a standard ICP algorithm of Chen and Medioni (1992) was chosen due to its efficiency. Their approach minimizes the point-to-plane error between corresponding points and allows two surfaces to slide against each other. In order to perform several hundreds of registrations in a reasonable time, the algorithm was modified to work on the GPU. Algorithmic details about the implementation are given in the A.

After registration, the average point-to-plane error Φ is stored along with each transformation. However, a fragment may match well at several positions due to the symmetrical shape of the bone template. As described in Papaioannou and Karabassi (2003), an approach minimizing the sum of matching errors among possible fragment combinations can be applied in such cases. Therefore, we propose to determine the best assembly by an accumulative error measure based on two criteria.

We use the overlap of fragments as an additional criterion for the quality of the assembly. In the ideal case, the affected and contralateral humerus are identical resulting in an assembly without any overlapping fragments. However, anatomical differences between the left and the right bone are often present in individuals, affecting the registration. Particularly, small differences in size must be taken into account due to intra-subject variation in the humeral head length (Delude et al., 2007). As exemplarily depicted in Fig. 5, the reconstruction based on a template of different size can result in gaps or overlapping fragments. Such scaling differences are not known a priori and, therefore, must be corrected after the contralateral reconstruction. The objective at this stage is the identification of the best reconstruction which, however, may contain gaps or intersections.

Therefore, an approach directly penalizing intersecting fragments is not appropriate in our case. Instead, we aim at finding the assembly that maximizes the covered area on the contralateral mesh as demonstrated in Fig. 5. The amount of covered area can be efficiently calculated by partitioning the contralateral mesh in dense cells using the already generated grid of the ICP registration. Each surface cell of the contralateral mesh which is hit by at least one of the fragments' points is marked as covered. The proposed overlapping error can be defined as the number of surface cells that are finally not covered. In case of marginal contralateral anatomical differences, the overlap error is minimal for the correct assembly and penalizes situations where fragments intersect as shown in Fig. 5a and b, respectively. In case of a smaller or larger contralateral humerus, the favorable assembly is among a set of assemblies with minimal overlap error since it covers the maximum grid area as outlined in Fig. 5c and d.

Finally, the most correct assembly is determined by evaluating all possible fragment configurations according to a measure that combines alignment and overlap error. $\prod_{i=1}^{N_F} 4 \cdot NC_{F_i}$ combinations have to be evaluated where N_F is the number of fragments. Since only good matches have to be considered for each F_i, transforma-

tions with an alignment error larger than $\mu_i + \sigma_i$ are not evaluated where μ_i is the average alignment error over the fragment's transformation set and σ_i the standard deviation, respectively.

On average 30 transformations remain per fragment which is an acceptable combinatorial effort in case of 4-part fractures. For each combination of transformations the error measure

$$\epsilon_{i,j} = \overline{\Psi}_j + \frac{1}{N_F} \sum_{i=1}^{N_F} \overline{\Phi}_{i,j} \tag{3}$$

is evaluated where $\overline{\Phi}_{i,j}$ is the normalized alignment error for the current transformation j of the ith fragment and $\overline{\Psi}_j$ denotes the normalized overlap error of the current combination including all fragments. Normalization (between 0 and 1) of Φ is performed per fragment whereas Ψ is normalized over all combinations. The final result is obtained by choosing the combination with minimal error according to Eq. (3).

4.2. Final reconstruction using fracture surfaces

Registration of fracture surfaces can be carried out if a good estimate of the correct fragment positions is known. In our approach the estimate is obtained by contralateral matching as described above. The fracture surfaces are determined by an extraction filter that will be outlined in Section 4.2.1. In Section 4.2.2 the actual registration is presented, consisting of two main steps, the pairwise registration of neighboring surfaces followed by a global multi-piece alignment.

4.2.1. Fracture surface extraction

Fracture surfaces of proximal humerus fragments are narrow. Our proposed filter particularly relies on this characteristics of a fragment to detect its fracture surface FS_i. The filter works locally on the point normals of the mesh within a filter range $\hat{\sigma}$ larger than the maximum fragment thickness. Mesh vertices x_j belonging to FS_i are found by iterating over all normals $\mathbf{n}_j$ and calculating the average angle between $\mathbf{n}_j$ and other normals in the $\hat{\sigma}$-range. We have tested $\hat{\sigma}$-values in the range of 2–4 mm – best results were achieved with $\hat{\sigma} = 3.5$ mm. A fixed radius search in a KD-tree (Mount and Arya, 1997) is carried out to determine all points within the $\hat{\sigma}$-radius. The filter function $F(x_j)$ is centered at x_j and has the form:

$$F(x_j) = \frac{1}{N_{\hat{\sigma}}} \sum_{x_j \in \hat{\sigma}, x_k \neq x_j} f(x_j, x_k) \tag{4}$$

$$f(x_j, x_k) = \begin{cases} |\angle(\mathbf{n}_j, \mathbf{n}_k)|, & \angle(\mathbf{n}_j, \mathbf{n}_k) > t_2 \\ 0, & \text{otherwise}. \end{cases} \tag{5}$$

where $\mathbf{n}_j$ denotes the normal of point x_j. $N_{\hat{\sigma}}$ is the number of points in the filter range for which Eq. (5) was nonzero. Two thresholds t_1 and t_2 are used to decide whether a point x_j is part of the fracture
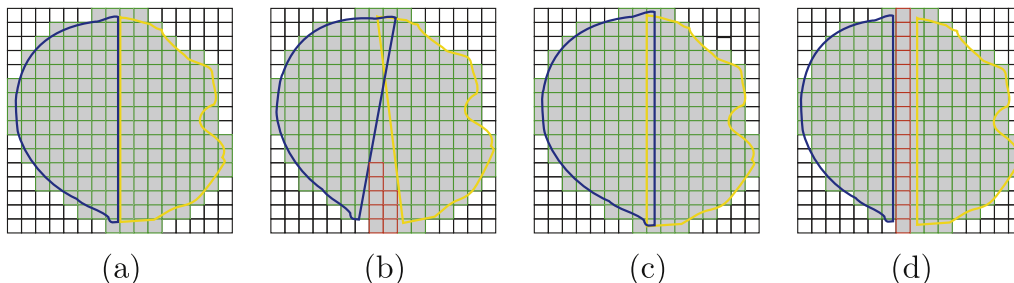

(a) (b) (c) (d)

Fig. 5. Examples of different overlap situations of two fragments which are outlined in yellow and blue, respectively. The uniform grid of the contralateral mesh is represented by grey cells. Cells covered by fragments are outlined in green and uncovered cells are colored red. Figure (a) and (b): No scaling differences between the left and the right side. Figure (c): Contralateral bone is smaller. Figure (d): Contralateral bone is larger. (For interpretation of the references to colour in this figure legend, the reader is referred to the web version of this article.)

surface. x_j is classified to be part of FS_i if the result of Eq. (4) is within $[\pi/2 - t_1, \pi/2 + t_1]$ where t_1 is a tolerance threshold. Threshold t_2 is used to distinguish between two cases:

$x_j \notin FS_i$ As shown in Fig. 6a, most normals point in both directions according to the two sides of the fragment. Without thresholding with t_2, approximately half of the normals have an angle similar to n_j while the rest of the normals point in the opposite direction. This would result in an average angle difference of approximately $\pi/2$ and n_j would be wrongly classified to the fracture surface. By applying threshold t_2, most normals similar to n_j are skipped resulting in an average angle $\gg \pi/2$.

$x_j \in FS_i$ In this configuration n_j is compared to the normals of the adjacent non-fractured regions as depicted in Fig. 6b and c. The threshold t_2 is used to avoid a biased result by skipping similar normals of the fracture surface. Two possible cases can be considered. (i) The fracture surface around n_j is orthogonal to the non-fractured regions as shown in Fig. 6b. In this case, most considered normals are nearly orthogonal to n_j and the average angle would ideally be $\pi/2$. (ii) The fracture surface is oblique to the non-fractured regions as depicted in Fig. 6c. Nevertheless, the average angle between n_j and the normals to both adjacent regions is approximately $\pi/2$ due to the fact that these regions are roughly parallel to each other within $\hat{\sigma}$. Therefore, a decrease in the angular difference between n_j and one region is compensated by an increased angle to the normals of the other region.

In case of high resolution data, threshold values of $t_1 = \pi/8$ and $t_2 = \pi/5$ were used. While the filter robustly identifies the fracture surface as demonstrated in Fig. 7a, a certain amount of false positives exist dependent on the smoothness of the shape. Therefore, a connected component analysis is performed for noise removal. Starting with the largest connected region, that is assumed to be part of the fracture surface, all regions, lying within a distance threshold of 0.2 mm, are merged. The connected regions are updated and the process is repeated until no more regions can be added. An example of the finally obtained fracture surface is given in Fig. 7b.

4.2.2. Pairwise registration and multi-piece alignment

Bone reassembling using fracture surfaces can be considered as a multi-view registration problem where partially overlapping parts or views of an object are aligned for full reconstruction. In our case a view is represented by a fragment and its fracture surface is the overlapping part that should be aligned as exactly as possible to adjacent fracture surfaces. Significant amount of re-
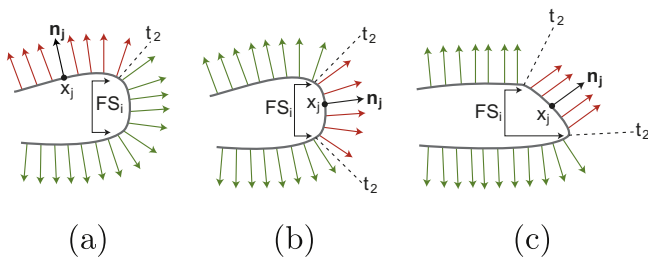

Fig. 7. Fracture surface extraction filter. (a) Filter result before connected component analysis. Correct fracture surface is shown in red. Regions to be removed are denoted in other colors. (b) Fragment overlaid with final result (red) after connected component analysis. (For interpretation of the references to colour in this figure legend, the reader is referred to the web version of this article.)

search was performed on multi-view registration. Most of the proposed methods perform the alignment of multiple views in a sequential or simultaneous fashion (Rodrigues et al., 2002). Regardless of the chosen approach, the relative transformation that correctly aligns two adjacent fragments must usually be estimated.

To this end, we first considered to use pairwise ICP registration of neighboring pieces to identify corresponding point pairs (Chen and Medioni, 1992; Masuda et al., 1996; Pulli, 1999). As Pulli pointed out, one of the difficulties in ICP is the definition of the part's overlap region that is intended to match with adjacent pieces. Most notably, ICP is known to fail in cases where the common overlap region between two objects is small. We have also experienced situations where two fragments initially intersected or were separated by several millimeters. In these cases, ICP converged to a wrong local minimum if the overlap region was small or inappropriately defined.

Therefore, we decided to apply a more robust registration method, better tolerating outliers and thus allowing an automatic and coarser definition of the overlap region. Our approach uses a kernel correlation-based registration proposed by Tsin and Kanade (2004). In a correlation-based method a point is multiply linked to several points in the other mesh and does not only rely on its closest point. The algorithm requires calculating the Gaussian kernel density estimator $P_i(\tilde{x}, \widetilde{T}_i)$ for each fracture surface FS_i

$$P_i(\tilde{x}, \widetilde{T}_i) = \frac{1}{\tilde{N}} \sum_{x_k \in FS_i} e^{-\|\tilde{x} - \widetilde{T}_i x_k\|^2 / \tilde{\sigma}^2} \qquad (6)$$

where parameter $\widetilde{T}_i$ denotes the current fragment transformation matrix and $\tilde{N}$ is a normalization factor defined in Tsin and Kanade (2004). We set the kernel scale to $\tilde{\sigma} = 10$. The density estimators are computed for each cell of a uniform grid with cell centers $\tilde{x}$ and a spacing of 1 mm. The grid size is defined by the bounding box covering the pair of fracture surfaces (FS_i, FS_j) which are targets for registration. (FS_i, FS_j) is registered by minimizing the cost function

$$KC(FS_i, FS_j) = -\sum_{\tilde{x}} P_i(\tilde{x}, \widetilde{T}_i) \cdot P_j(\tilde{x}, \widetilde{T}_j). \qquad (7)$$

which corresponds to minimizing the distance between the points of FS_i and FS_j. The registration is robust to outliers since the summation term of Eq. (6) decreases exponentially with increasing point distances. A nonlinear optimization based on a derivative-free bundle method (Beliakov and Ugon, 2007) is used to iteratively minimize Eq. (7) with respect to $\tilde{T}_i$. The optimization result after l steps is denoted by $\min_{\tilde{T}_i} KC_l(FS_i, FS_j)$.

Fig. 6. 2-d example of the fracture surface extraction approach. The filter is centered at point x_j having normal n_j. Red colored normals are skipped by threshold t_2 according to Eq. (5). Remaining normals are colored in green. (a) Case: $x_j \notin FS_i$. (b) Case: $x_j \in FS_i$, orthogonal fracture surface. (c) Case: $x_j \in FS_i$, oblique fracture surface. (For interpretation of the references to colour in this figure legend, the reader is referred to the web version of this article.)
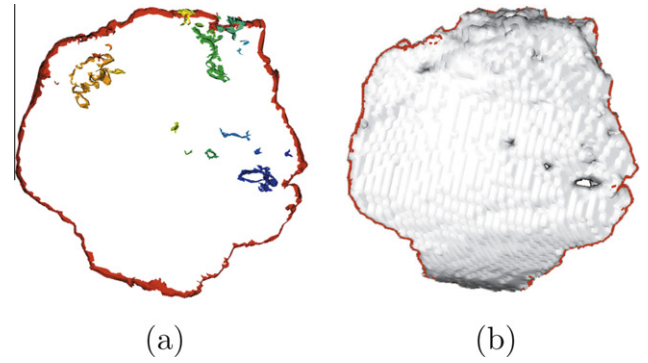
Although correlation-based registration is very robust, the overlap region of the two fracture surfaces has still to be coarsely estimated. In our approach this is automatically performed. To this end, point subsets are created based on the minimum distance $d_{min}(FS_i, FS_j)$ between FS_i and FS_j. Subset $S_i(FS_j, d)$ contains all points of FS_i having a maximum distance of $d_{min}(FS_i, FS_j) + d$ to FS_j. Each pair (FS_i, FS_j) is registered as follows.

Algorithm 1. Correlation-based fracture surface registration

initialize $\widetilde{T}_i, \widetilde{T}_j$ with estimates obtained from contralateral matching
$k \leftarrow -1$
$d \leftarrow 5$
$\epsilon_i^k \leftarrow \infty$
$\epsilon_j^k \leftarrow \infty$
repeat
$\quad \epsilon_i^{k+1} = \min_{\widetilde{T}_i} KC_{l=15}(FS_i, FS_j)$
$\quad \epsilon_j^{k+1} = \min_{\widetilde{T}_j} KC_{l=15}(FS_j, FS_i)$
$\quad d \leftarrow \min(3, d-1)$
$\quad update(S_i(FS_j, d))$ {update subset S_i according to d}
$\quad update(S_j(FS_i, d))$ {update subset S_j according to d}
$\quad k \leftarrow k+1$
until $\left|\epsilon_i^k - \epsilon_i^{k-1}\right| + \left|\epsilon_j^k - \epsilon_j^{k-1}\right| \leqslant \delta$

In each kth iteration FS_i and FS_j are symmetrically registered where the optimization result is denoted by ϵ_i^k and ϵ_j^k, respectively. After $l = 15$ optimization steps, the distance d is decreased and the subsets are updated according to the current minimum distance. The value of l has been determined experimentally. The algorithm is repeated until the relative change of ϵ_i and ϵ_j between two iterations falls below a threshold $\delta = 0.01$.

After convergence, the set of constraining point pairs is created. We consider pairs $(\widetilde{T}_i x_k \in FS_i, \widetilde{T}_j x_l \in FS_j)$ with a distance error smaller 0.5 mm since the overlap is usually not perfect and points do not coincide. However, distance errors can bias the subsequent multi-piece alignment since it relies on calculating transformations based only on these point pairs. To avoid accumulation of pairwise errors in the multi-piece alignment, we use the ideal mates concept which is explained in detail in Pulli (1999), instead of taking the specific pairs $(\widetilde{T}_i x_k, \widetilde{T}_j x_l)$ as depicted in Fig. 8a. The approach requires to calculate the relative transformation $\widetilde{T}_{i \to j}$ between registered pieces F_i and F_j with transformations $\widetilde{T}_i$ and $\widetilde{T}_j$, respectively. An ideal mate of a point $\widetilde{T}_i x_k \in F_i$ is the point $\widetilde{T}_j \widetilde{T}_{i \to j} x_k$ which defines where $\widetilde{T}_i x_k$ should appear in the coordinate system of F_j. In the ideal case of the subsequent multi-piece alignment the orientation between F_i and F_j is equal to the transformation $\widetilde{T}_{i \to j}$, resulting in a perfect correspondence of the point pairs

with no alignment error. However, fragment transformations T_i^* during multi-piece alignment typically differ from the pairwise registration result since the point pair constraints between all fragments are considered. In this case the ideal mate concept allows to calculate the multi-piece alignment error without relying on the pairwise registration error as demonstrated in Fig. 8b. The set of constraining point pairs for F_i, describing the optimal alignment of F_i to F_j, is defined as

$$\mathscr{C}_{i,j} = \{(\widetilde{T}_i x_k, \widetilde{T}_j T_{i,j} x_k) : \|\widetilde{T}_i x_k - \widetilde{T}_j x_l\| \leqslant 0.5 \land x_k \in FS_i \land x_l \in FS_j\}.$$

The described pairwise registration is applied to all neighboring fragments. We define two fragments to be neighbors if at least 10% of their fracture surface points are within a neighbor-distance of 4 mm after contralateral matching.

In the last step, the final global alignment is carried out. First, we tested approaches where the pieces were sequentially aligned (Chen and Medioni, 1992; Masuda et al., 1996; Okada et al., 2009). However, these methods resulted in inaccuracies due to accumulation of registration errors (Rodrigues et al., 2002).

Therefore, we finally relied on a simultaneous alignment method based on the work of Pulli (1999). The basic idea is to iteratively calculate fragment transformations T_i^* that optimally enforce all pairwise registration constraints. To this end pieces are consecutively added to a growing set of already aligned objects (i.e. active set $\mathscr{A}$) while keeping the objects of the set correctly aligned. A backtracking mechanism allows to simultaneously align all fragments in $\mathscr{A}$ until consistency.

In our case the algorithm starts by putting the shaft fragment F_0 into $\mathscr{A}$ while all other pieces remain in the inactive set $\mathscr{I}$. Thereafter, the fragment that contains most points within neighbor-distance to $\mathscr{A}$, is removed from $\mathscr{I}$ and inserted in $\mathscr{A}$. The pieces of the active set are then aligned as described by Pulli (1999) and the overall process is repeated until the inactive set is empty. Our method differs from the original algorithm in two aspects. First, F_0 is kept fixed to prevent unstable movement of the overall data set in case of a circular dependency between fragments. Second, a point pair selection strategy for the fragment alignment to the active set is introduced. Basically, a fragment F_i is aligned to $\mathscr{A}$ by minimizing the distance between point pairs

$$\left(T_i^* x_k, T_j^* \widetilde{T}_{i \to j} x_k\right) \in \bigcup_{j:F_j \in \mathscr{A}} \mathscr{C}_{i,j} : \mathscr{C}_{i,j} \neq \emptyset \land x_k \in FS_i$$

where T_i^* and T_j^* are the current transformations of F_i and F_j in the multi-piece alignment. The transformed pairs are used to solve the absolute orientation problem (Horn, 1987). However, incorrect point pair correspondences can still exist in the point pair set which limit the global alignment. Our approach automatically rejects such suspicious point pairs. To this end $\xi \cdot N_{\mathscr{C}}$ closest point pairs are chosen out of all $N_{\mathscr{C}} = |\bigcup \mathscr{C}_{i,j}|$ pairs. Parameter ξ is determined by minimizing the error function (Chetverikov et al., 2002)
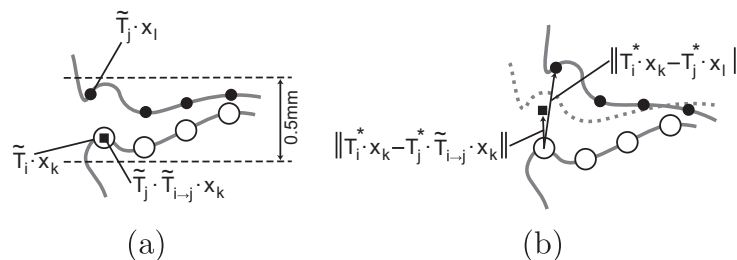

Fig. 8. (a) Point pair generation after pairwise registration. The concrete mate of point $\widetilde{T}_i x_k$ (white circle) is the closest point $\widetilde{T}_j x_l$ (black circle). The ideal mate (black square) is defined as $\widetilde{T}_j \widetilde{T}_{i \to j} x_k$. (b) In the multi-piece alignment, the distance error $\|T_i^* x_k - T_j^* \widetilde{T}_{i \to j} x_k\|$ based on ideal mates is not biased by the pairwise registration error in contrast to the error $\|T_i^* x_k - T_j^* x_j\|$ between concrete pairs.

$$\psi(\xi) = \frac{e(\bigcup_j \mathscr{C}_{i,j}, \xi)}{\xi^\lambda} \tag{8}$$

$$e\left(\bigcup_j \mathscr{C}_{i,j}, \xi\right) = \frac{1}{\xi N_{\mathscr{C}}} \sum^{\xi N_{\mathscr{C}}} \|T_i^* x_k - T_j^* \widetilde{T}_{i \rightarrow j} x_k\|^2 \tag{9}$$

where e is the trimmed mean squared error. We set $\lambda = 3$ to penalize smaller ξ values and bound ξ to the range [0.8, 1.0]. Brent's method (Press et al., 2002) is used to calculate the minimum of Eq. (8). This selection strategy allowed faster convergence with a slightly smaller final error (in the range of 0.2 mm) compared to a rejection based on standard deviation of the distances.

5. Results

The feasibility of our approach was initially evaluated on artificially created fractures on cadaver humeri. A Philips Brilliance 40 CT scanner (Philips Healthcare, Best. NL) was used for data acquisition. Afterwards, the performance of the method was tested on clinical cases.

5.1. Cadaver experiments

For the cadaver experiments two fresh-frozen pairs of humeri without any evidence of previous surgery or trauma were used. First, CT data of the four unfractured humeri were acquired. Thereafter, each proximal humerus was fractured by blunt impact after creation of cortical bone stress concentrations using a 2 mm surgical drill and surgical chisel. The small mechanical defects (<4 mm) were placed by an experienced orthopedic surgeon at the proximal intertubercular groove, the inferior margin of the greater tuberosity and at the medial edge of the surgical neck. After the defects were placed, the humeral shaft was rotated in the transverse plane 30° from perpendicular with the humeral head in contact with a thin piece of polyurethane foam mounted to a rigid surface. The bone was then impacted at the distal extreme using a 1 kg steel mallet, transferring load along the humeral shaft to the head. Impacts were repeatedly delivered until at least three fragments were obtained. In two cases, fracture could not be initiated using this approach, and the humeral head was then directly impacted along an axis rotated in the transverse plane approximately 30° oblique to the humeral shaft. Manual palpation and examination of the fragments by the surgeon confirmed that while severe, the fractures and the fragment geometry were representative of those clinically observed. The imposed mechanical defects did not introduce any obvious fiducial landmarks that would benefit registration. Volume rendered CT images of the cadaveric specimen before and after fracturing are given in Fig. 9.

5.1.1. Accuracy

CT scans have been acquired using two different axial resolutions of 0.67 mm and 1 mm, respectively. This allowed testing the performance of our method with high as well as low resolution data. The latter being comparable to typical clinical acquisitions. The computer assisted planning was carried out for each scan specified in Table 1. In order to evaluate the accuracy of the approach, the correct fragment position in the originally unfractured bone could be used as ground truth. Unfortunately, this information has not been directly available and had to be estimated by determining the transformation applying multiple registrations as described in Section 4.1.2 without including any overlapping constraints between fragments. Registration was performed using the GPU-ICP implementation as well as a CPU version, yielding equal results. The accuracy of the ground truth was assessed by the fiducial registration error (FRE) (Fitzpatrick et al., 1998). The highest FRE of a fragment was 0.25 ± 0.1 mm and 0.27 ± 0.14 mm
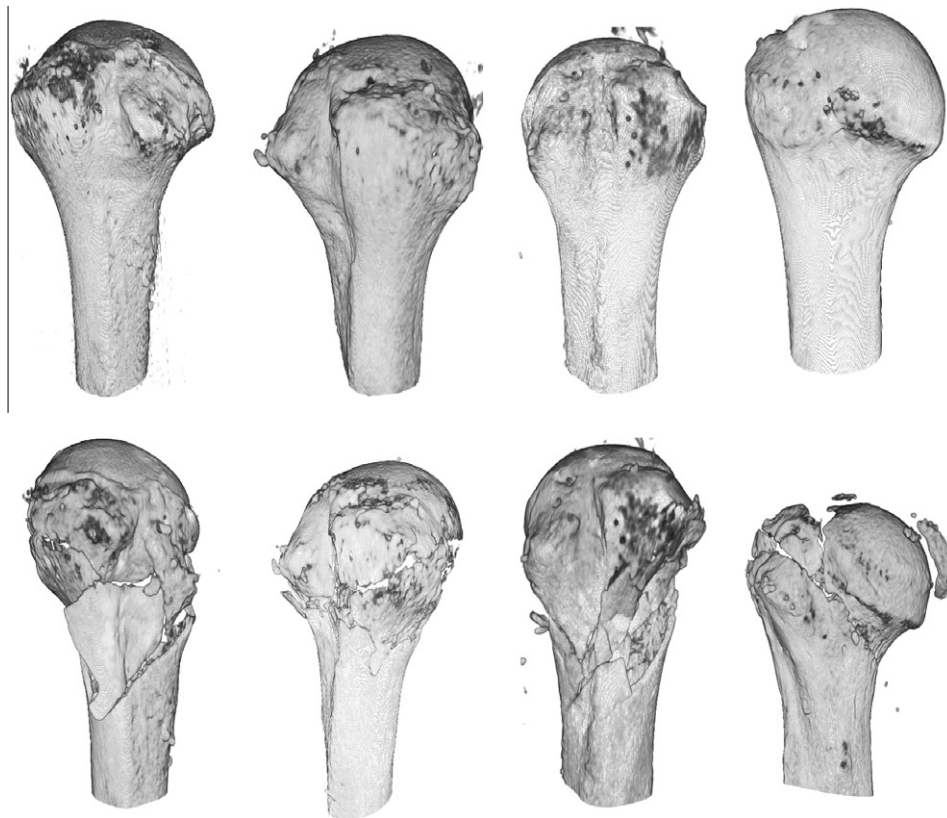

Fig. 9. Volume rendering of the cadaver humeri. Top row: Unfractured bones. Bottom row: Corresponding humeri after fracturing.

Table 1
Overview of the performed experiments using two pairs of cadaver humeri denoted by C1 and C2, respectively. The experimental data were acquired in two different resolutions. The → symbol connects the humerus that is target for reconstruction and the contralateral humerus acting as the template, respectively.

Experiment	Resolution x/y, thickness/spacing (mm)	Mesh size unfractured (# points)	# Fragments
1: C1 *left → right*	0.29/0.29, 0.67/0.33	290,450	5
2: C1 *right → left*	0.29/0.29, 0.67/0.33	503,400	5
3: C2 *left → right*	0.29/0.29, 0.67/0.33	367,690	3
4: C2 *right → left*	0.29/0.29, 0.67/	361,370	4

in Experiments 1–4 and Experiments 5–8, respectively. The mesh points of the fracture surfaces were not included in the computation of the FRE.

The ground truth position of each fragment was compared to the result of our method after contralateral and final assembly as shown in Table 2. The translational error was defined as the Euclidean distance of the fragment center in ground truth and reconstructed position. The rotational errors α and β were calculated based on the angular differences of the fragment's three 2nd moment vectors in reconstructed and ground truth position. α denotes the maximum rotational difference around the two largest moment vectors. Correspondingly, β represents the rotational difference around the smallest 2nd moment vector. The β error quantifies the in-plane rotational error of the fragment on the reconstructed bone surface while the α value has a stronger effect on the overall shape of the reconstructed bone.

5.1.2. Contralateral anatomical differences

Side-to-side variabilities of both unfractured cadaver pairs were measured in order to study correlations between anatomical differences of the sides and the reconstruction accuracy of our algorithm. To this end the proximal shaft part of one specimen was virtually separated from the head at the surgical neck and registered to the opposed mirrored bone. The transformation obtained from this registration was then applied to the head part in order to align both heads with respect to their shafts.

Closest point distances between the heads were evaluated and visualized in Fig. 10. An average distance error of 0.73 ± 1.12 mm was measured for the first pair. Several regions showed differences up to 3 mm. The second pair had a smaller variability of 0.47 ± 0.38 mm on average. The maximum diameter of the head including the greater and lesser tuberosity, was almost identical for both pairs. For cadaver pair 1 diameters of 55.4 mm and 54.9 mm were measured for the left and right side, respectively. In case of cadaver pair 2, the diameters of the left and right head were 56.6 mm and 56.7 mm. The measurements were obtained by fitting a sphere to the mesh vertices of the head in a least-squares sense (Schneider and Eberly, 2002).

5.2. Clinical cases

In addition to the accuracy evaluation in the cadaver experiments, the method was tested on four clinical data sets.[1]

An overview of the cases is given in Table 3 as well as in Fig. 11. The performance of the reassembly was assessed by the quality of the contact along the fracture surfaces as well as by the smoothness of the reconstructed bone surface at the interface of adjacent fragments.

The quality of the contact was expressed by the contact ratio C_r as described in Okada et al. (2009). The proposed measure quantifies gaps and intersections at evaluation points sampled along the fracture surfaces. We have used sampling intervals of 5 mm. For each evaluation point, the surface patch inside a small sphere (i.e. 5 mm radius) was analyzed. If an intersection between fragments was detected within the radius, we defined the intersection error as the maximum of the closest-point distances between the intersecting fracture surfaces. Otherwise, the gap error was defined as the minimum distance between the surface patches of the fragments. Finally, C_r was specified as the ratio of the number of evaluation points where both errors were below 3 mm, divided by the total number of evaluation points.

The reconstructed bone surface should be smooth without discontinuities, as steps or sharp bending at the contact interface between pieces. In our evaluation we defined the contact interface as the set of surface points where the inter-fragment distance was less than 1 mm. The smoothness was locally measured at evaluation points which were sampled along the contact interface in 5 mm intervals.

To obtain the correct surface connectivity at fragment boundaries, all pieces were combined into a single mesh. To this end, a sampled implicit model (Schroeder et al., 1994) was generated with an isotropic sampling resolution of 0.5 mm. The merged triangle mesh was subsequently constructed from the zero level set of this implicit model using the marching cube algorithm (Lorensen and Cline, 1987). Thereafter, surface patches of 4×4 mm were created from the connected neighborhood around each evaluation point. Optimally, the transition between fragment boundaries is seamless and the extracted patch is locally flat. Therefore, the local curvature of the patch, estimated by the flatness measure (Mederos et al., 2005)

$$s = \frac{\lambda_1}{\lambda_1 + \lambda_2 + \lambda_3},$$

was used as a quality criterion. The values $\lambda_1 \leqslant \lambda_2 \leqslant \lambda_3$ denote the eigenvalues obtained from a covariance analysis of the points. Similar to the contact ratio, the smoothness ratio S_r was defined as the

Table 2
Accuracy evaluation of the cadaver experiments. Average fragment error is defined as the translational difference (in mm) and rotational error (in degree) to the ground truth. α denotes the maximum rotational difference around the two largest moment vectors. β represents the rotational difference around the smallest 2nd moment vector. Errors are given for contralateral assembling and for the finally reconstructed bone using fracture surfaces.

Experiment	Contralateral assembling error		Final reconstruction error	
	Translational (mm)	Rotational (°)	Translational (mm)	Rotational (°)
1	3.02 ± 0.8	α = 7.1 ± 2.6, β = 5.1 ± 3.0	1.06 ± 0.35	α = 2.5 ± 1.5, β = 3.5 ± 1.18
2	2.92 ± 1.13	α = 2.4 ± 1.5, β = 3.5 ± 2.1	1.13 ± 0.34	α = 1.5 ± 0.8, β = 3.1 ± 2.1
3	1.22 ± 0.41	α = 3.1 ± 0.4, β = 2.5 ± 1.6	0.90 ± 0.50	α = 2.5 ± 0.8, β = 2.8 ± 2.0
4	1.56 ± 0.69	α = 3.4 ± 2.8, β = 3.8 ± 2.3	1.11 ± 0.59	α = 2.1 ± 1.9, β = 2.6 ± 1.7
5	3.78 ± 0.28	α = 7.0 ± 4.0, β = 8.1 ± 3.1	1.37 ± 0.29	α = 3.5 ± 2.5, β = 5.5 ± 3.3
6	2.10 ± 0.45	α = 4.9 ± 3.5, β = 6.1 ± 4.9	1.26 ± 0.43	α = 3.6 ± 2.0, β = 3.0 ± 0.3
7	2.00 ± 0.14	α = 5.1 ± 0.8, β = 3.4 ± 1.4	0.4 ± 0.60	α = 5.4 ± 0.4, β = 5.1 ± 2.6
8	2.67 ± 1.0	α = 4.7 ± 5.1, β = 3.5 ± 1.8	1.63 ± 0.64	α = 3.7 ± 2.9, β = 2.5 ± 2.1

---

[1] The further use of the clinical image data for such investigations was approved with waiver of informed patient consent by the responsible Ethics Committee.
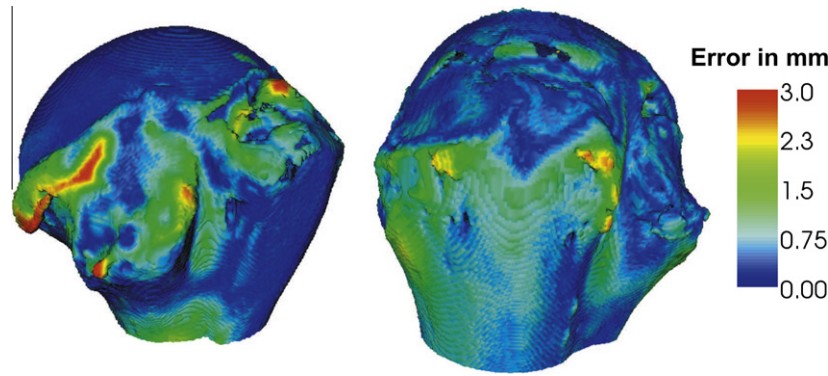
Fig. 10. Side-to-side variabilities of cadaver pair 1 (left) and cadaver pair 2 (right), respectively.

Table 3

Clinical data sets. CT image resolution, mesh size of the contralateral bone and number of fragments is given. The quality of the contact between fragments and the smoothness of the fracture site after reconstruction is given by the ratios C_r and S_r, respectively.

Case	Resolution x/y, thick./spacing (mm)	Mesh size unfract. (# points)	# frag.	Contact ratio C_r	Smoothness ratio S_r
1	0.35, 0.9/0.45	127,000	3	0.91	0.93

number of evaluation points where $s < s_{max} = s_\mu + 2s_\sigma$, divided by the total number of evaluation points. s_μ and s_σ denote the mean smoothness of the contralateral mesh and its standard deviation, respectively. These values were obtained by averaging the flatness values of smooth surface patches not containing sharp edges. The contact and smoothness ratios for each case are provided in Table 3. Both ratios should be one for optimal reconstruction.

In all four cases, at least 85% of the evaluation points had a contact error below 3 mm. The best contact quality was measured in case 2 where all evaluation points fulfilled the criterion. In case 1, one fragment was too small to be considered in the reassembly. Similarly, two very small fragments were not included in the reconstruction of case 4. In these two cases, the contact ratio was only measured at evaluation points between the fragments included in the planning. The evaluation of the smoothness quality showed a similar trend. On average, the flatness of the surface patches was below the tolerance s_{max} in 93% of the evaluation points. The value of s_{max} derived from the contralateral surface was very similar among the four cases. s_μ and s_σ ranged within 0.018–0.02 and 0.013–0.026, respectively.

5.3. Runtime

We have evaluated the efficiency of each step of the algorithm for all presented experiments and clinical cases. The runtime is given in Tables 4 and 5. In the preprocessing step, the initial transformations based on candidate points are calculated as described in Section 4.1.1. The GPU version of ICP was compared to a CPU implementation using a KD-tree (Mount and Arya, 1997) where the contralateral matching for each fragment was executed in a separate thread.

6. Discussion and outlook

The results of the cadaver experiments clearly show the accuracy of our approach. In experiments with high resolution CT data

the average fragment displacement error compared to the ground truth was 1.0 ± 0.4 mm and $2.8 \pm 1.1°$. Similar errors of 1.3 ± 0.4 mm and $3.4 \pm 2.2°$ were obtained in case of lower resolution. This demonstrates that the algorithm can be applied to clinical cases where CT images with lower resolutions are acquired. Nevertheless, the rotational error was significantly higher in all experiments, compared to the measurements with high resolution data. One reason might be the less accurate fracture surface extraction. Due to the flatness of fracture fragments, the rotational part of the registration is much more susceptible to inaccuracies compared to the translation.

The average error after contralateral assembly was 2.2 ± 1.1 mm and $5.3 \pm 2.9°$ in Experiments 1–4, and 2.7 ± 0.9 mm and $6.6 \pm 3.3°$ for Experiments 5–8 with a maximum error of 4 mm and 10°. These results show that the proposed contralateral matching can be used to reassemble humerus fractures. However, the method requires an additional CT scan of the uninjured humerus which increases the patient's radiation exposure.

Registration with the contralateral bone only based on the initial fragment position may fail in case of larger displacements due to the featureless geometry of the humerus head. Previously performed tests, including additional features like CT image intensity or curvature (Sharp et al., 2002), did not improve robustness as these were not sufficiently discriminative to overcome wrong local minima. Our approach therefore uses multiple initializations for each fragment and selects the best assembly according to the introduced error measure. An independent registration of the fragments without incorporating the overlap was not robust, since some fragments yielded excellent matches on several positions. However, even the best match to the contralateral bone provided suboptimal results. One reason may be anatomical differences between left and right, which was visualized for both cadaver pairs in Fig. 10. This assumption is supported by a study of Delude et al. (2007), demonstrating a considerable contralateral variability of the humeral head length and differences in the head retroversion angle. We have observed that the contralateral registration showed larger errors in case of cadaver pair 1 where higher side-to-side variability was measured. Additionally, small scaling differences between the left and the right humerus can be assumed for this cadaver pair. In Experiment 1 the fragments did markedly intersect after contralateral registration as demonstrated in Fig. 12a. Correspondingly, Experiment 2 showed gaps between the fragments, caused by contralateral matching to a possibly larger bone. Consistent results were obtained using the low resolution data.

As a consequence, our approach refines the initial assembly by a direct alignment of the fracture surfaces without relying on the contralateral bone template. A correlation-based algorithm allowed a very coarse definition of the regions being target for registration due to the robustness of the method. Symmetric regis-
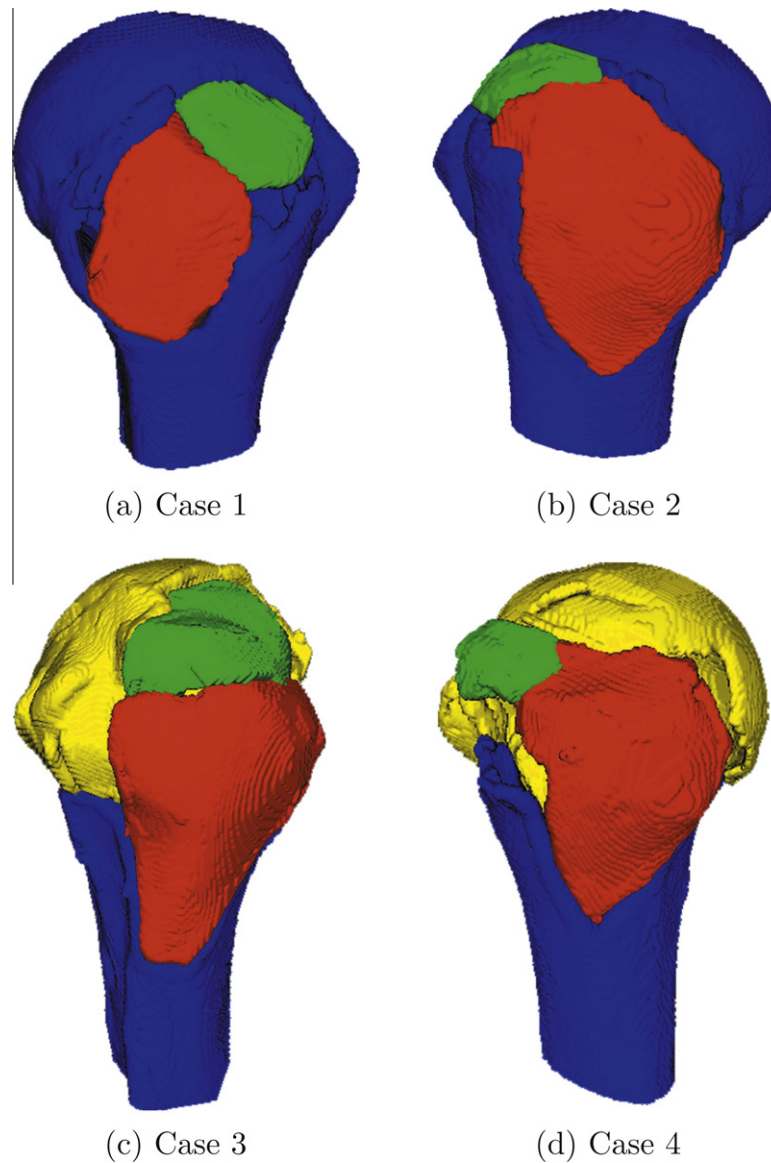
(a) Case 1   (b) Case 2

(c) Case 3   (d) Case 4

Fig. 11. Reconstructed clinical cases.

Table 4
Runtime of the reconstruction algorithm in seconds on a P4 3.2 GHz, NVIDIA GeForce 9600 GT machine. Timings for preprocessing and contralateral assembly are given in seconds.

Data set	Preprocessing (s)	Contralateral assembly (s)	
		Registration GPU (CPU)	Error measure & overlap test GPU (CPU)
Exp. 1	44	590 (11,118)	57 (435)
Exp. 2	36	343 (7636)	39 (549)
Exp. 3	42	249 (4578)	0.5 (12.8)
Exp. 4	45	359 (6493)	1.7 (26)
Exp. 5	42	376 (8432)	36 (280)
Exp. 6	28	204 (4298)	34 (281)
Exp. 7	30	132 (4171)	0.2 (2.5)
Exp. 8	31	118 (4451)	0.2 (10)
Clin. 1	16	48 (400)	0.5 (5.7)
Clin. 2	15	58 (454)	0.7 (7.9)
Clin. 3	15	175 (6062)	1.5 (11.8)
Clin. 4	11	110 (4200)	0.7 (4.0)

Table 5
Runtime of the reconstruction algorithm in seconds on a P4 3.2 GHz, NVIDIA GeForce 9600 GT machine. Timings for fracture surface extraction, pairwise registration, and multi-piece alignment are given in seconds.

Data set	Fracture surface assembly (s)		
	Extraction filter Filter	Pairwise Registration GPU (CPU)	Multi-piece Alignment
Exp. 1	92	549 (1100)	6.5
Exp. 2	111	867 (817)	6.4
Exp. 3	50	260 (349)	2.7
Exp. 4	44	288 (350)	2.4
Exp. 5	36	500 (925)	5.5
Exp. 6	35	445 (612)	5.6
Exp. 7	32	305 (480)	2.2
Exp. 8	27	259 (298)	0.2
Clin. 1	10	200 (212)	0.4
Clin. 2	6	204 (231)	0.3
Clin. 3	13	384 (511)	3.8
Clin. 4	11	368 (451)	4.8

tration with a stepwise reduction of the region of interest improved the overall robustness, especially in case of missing pieces

between fragments. While the accuracy of the final assembly was excellent in experiments, opposing fracture surfaces did not match
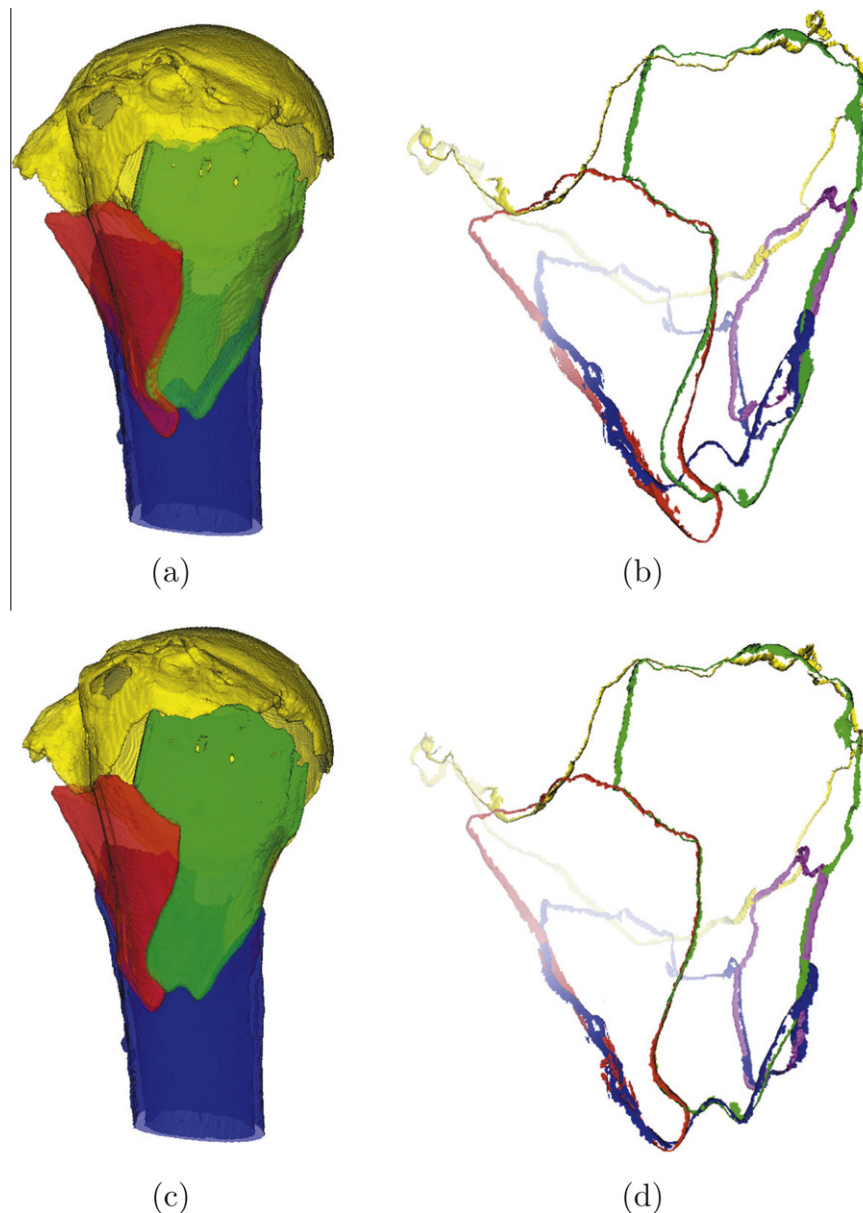
Fig. 12. Bone reconstruction steps of Experiment 1. Fragments were rendered transparent to show intersections between pieces. In Figures (b) and (d) computer-generated fog was added to improve depth perception. (a) Result after contralateral assembly. (b) Result of fracture surface extraction after contralateral assembly. (c) Final result after alignment of fracture surfaces. (d) Finally aligned fracture surfaces.

perfectly. One reason might be the challenging segmentation of these thin-walled fragments as well as difficulties in precisely extracting the fracture surfaces. Further research is planned to improve their quality, which would particularly improve the rotational registration. The applied iterative multi-fragment alignment distributes the pairwise registration error evenly among all pieces. The problem of collective sliding of the fragments, which was observed in some experiments, was solved by keeping the shaft fragment fixed during alignment. Incorrect point pair correspondences of the pairwise registration biased or slowed down the alignment process. The evaluation of the trimmed mean square error defined in Eq. (8) allowed to automatically remove suspicious point correspondences which results in faster convergence and a smaller error.

The computational efficiency of the algorithm is a clinically important factor, as it significantly influences the overall planning time. The presented method is computationally demanding but the

planning can be performed in a reasonable time by executing the most expensive parts on the GPU. The contralateral matching approach is only practicable if a very efficient but accurate registration method is applied. Our proposed GPU implementation, described in detail in the A, allows huge speedup compared to a standard CPU implementation with a KD-tree which is inefficient in case of large meshes. On the GPU, the registration can be efficiently performed using all mesh points without reducing the mesh size. Previously we have tested mesh decimation algorithms (Lindstrom, 2000; Schroeder et al., 1992) and point selection strategies (Rusinkiewicz and Levoy, 2001) on the CPU to improve efficiency. However, it was not possible to find an approach that significantly reduced runtime in all experiments. Most time-consuming is the contralateral matching of large fragments since at least 32 registrations are tested according to Eq. (2). It is difficult to automatically define the number of required registrations for varying fragment sizes. Our strategy was to overestimate the

number of candidate points necessary to determine the most correct assembly. A manual initialization of large fragments with pronounced landmarks or a more constrained search space would therefore allow reducing the runtime. However, our aim was to demonstrate that this step can be performed without user interaction and without additional constraints like a limited region of interest. A smaller speedup was achieved for the typically expensive correlation-based registration. Fracture surface meshes are small-sized which makes a parallelization less effective. For the overlap calculations, the runtime is acceptable for fractures with up to five parts although the combinatorial effort increases significantly compared to 3- or 4-part fractures. However, usually only fractures with less than five fragments are treated by open reduction (Wijgman et al., 2002). A reconstruction which includes more than five pieces would require to reduce the number of possible combinations. This could be achieved by a hierarchical overlap test that merges already consistent fragment transformations to groups. Alternatively, a dynamic programming approach could be used (Papaioannou and Karabassi, 2003).

Additional speedup is possible if only relevant point subsets would be used for testing. The overall assembly time is mainly dependent on the resolution of the CT image, the size of the fragments and the complexity of the fracture. The computational effort is much lower in case of simple fractures with small fragments like in clinical cases 1 and 2.

In comparison to our previously described interactive assembly system (Harders et al., 2007), the proposed method has the advantage that the manual identification of correspondences between displaced fragments can be avoided by performing the contralateral-based reconstruction in an automatic fashion. This task can be very challenging if performed interactively. Furthermore, the manual alignment of adjacent fracture surfaces requires extensive manual effort. In comparable cases, the interactive planning task was carried out in 15–30 min by an experienced operator.

Compared to the approach of Okada et al. (2009), our method has clear advantage in several aspects but also drawbacks. Their registration method can handle fragment displacement up to a certain degree but it still relies on the initial position of fragments. Even if for femur treatment planning the maximum displacement was limited to 2 cm and 30°, several incorrect registrations were still observed in their experiments. In our case the maximum displacement that may occur clinically might be higher – a significant dislocation is defined by a displacement of at least 1 cm or 45° in literature (Neer, 1970, 2002). Our contralateral matching algorithm performs the registration completely independent on the fragment displacement. This was clearly demonstrated in the presented cases which were successfully assembled without relying on the initial configuration. For global alignment, Okada et al. consecutively applied ICP registration against a set of already aligned objects. We have evaluated the performance of Okada's method on the the cadaver data in high resolution. The alignment of the fracture surfaces was applied *after* the contralateral matching step described previously. Therefore, the fragment displacement can be considered as small (see Table 2). The method of Okada et al. could register the fracture surfaces if the order of alignment as well as the corresponding overlap regions were appropriately chosen. The alignment order had to be defined such that the overlap between the current fragment and the aligned set was sufficiently large. Additionally, the definition of corresponding overlapping regions required fine-tuning in several cases. The final alignment error was higher in all four experiments. Compared to the ground truth, the average error in Experiments 1–4 was 2.0 ± 0.4 mm and $4.8 \pm 1.3°$ using the method of Okada et al. Sequential alignment is known to accumulate registration errors (Rodrigues et al., 2002) which might be one reason for the higher error. Additionally, ICP registration of thin fracture surfaces may be more er-

ror-prone than correlation-based registration. It must be noted that Okada et al. proposed different combinations of the registration process (see Section 2) but only the global registration of fracture surfaces was evaluated to allow a direct comparison with our alignment approach. The main drawbacks of our approach compared to Okada's method are the significant higher runtime and the larger number of user-defined parameters.

6.1. Limitations

Currently, we discard smaller fragments during the planning process. All fragments, where the sum of the mesh triangles' area is smaller than 1000 mm^2, are automatically removed by the algorithm, since contralateral matching did not robustly work for them. Removed fragments had a maximal length of less than 1.5 cm on average. In the cadaver experiments not even the correct position on the original bone could be determined to generate a ground truth. However, reconstruction by open reduction is typically performed on fractures with larger pieces. Nevertheless, the integration of very small fragments is planned in the future in order to evaluate possible gains in accuracy.

Some algorithmic parts required manual interaction in the tested cases. The automatic determination of the moment vector direction used to generate initial fragment positions may fail for planar or concave-shaped fragments. While typical fragments are convex-shaped, the direction of $\mathbf{e}_3$ had to be manually flipped in three cases. Additionally, the neighborhood of adjacent fragments is currently only defined by their distance. In one complex case the correct neighborhood of three fragments was defined by the user since all pieces overlapped in the same region.

Fracture surface extraction required user-controlled correction in order to remove incorrect parts not belonging to the fracture surface. In such cases, the noisy regions were separated from the fracture surface and the connected component analysis was repeated.

Finally, another important issue is the optimal selection of the user-defined parameters. Manual adjustment of these values may be necessary in a larger series of fractures. Further research will focus on the development of strategies for adaptive parameter selection.

6.2. Parameter selection

Our method relies on user-defined values which were determined experimentally based on the data available. Several parameters might require adaption in a larger series of patients to account for the wide range of possible fractures and anatomy. Therefore, a discussion of parameter-depending effects on the reconstruction is provided in this section.

The process of model generation comprises fragment segmentation and separation from CT images. The quality of the region growing segmentation is primarily dependent on the bone enhancement filter which demonstrated high accuracy in detecting bone structures (Descoteaux et al., 2006). In the separation method, the definition of hard constraints is the only factor relying on user-defined values. While the position of the seed points has no direct influence on the separation, the size of the region in which the hard constraints are defined must be chosen appropriately large. For instance, more hard constraints are required to enforce the correct separation in cases of fragments which are densely connected. Contrary, the size must not be larger than the fragment itself. We have chosen a relative small region size (i.e. 5 mm) while relying on a larger number of hard constraints by placing additional seeds.

In the pre-processing stage described in Section 4.1.1, ray casting is applied to identify the outer bone surface. Our experiments

have shown that the outer surface extraction is robust to a wide range of parameter values (i.e. $\Delta t = 5 - 25$ mm) due to the following reason. Inappropriate offset values result only in an increase of false positives. Most of these regions are automatically removed by the subsequent connected component analysis. Eventually still remaining erroneous detections result in redundant candidate points not affecting the best assembly.

The number of candidate points per fragment are determined by Eq. (2). The primary reason of using an adaptive procedure is the improved runtime performance. While over-sampling has no influence on the contralateral reconstruction, an insufficient amount of candidate points may result in decreased accuracy. An evaluation in a larger series of patients is required to confirm whether the defined step function can robustly deal with all cases. Additionally, user control of this process would allow to increase the sampling in critical areas or completely leave the generation in certain areas out of consideration.

The best contralateral assembly is determined by evaluating the error measure given by Eq. (3). In our experiments, equal weighting between alignment and overlap error resulted in correct reconstructions. Nevertheless, a different weighting scheme might be required for other data sets since the significance of the individual terms of the equation is dependent on the fragment sizes as well as on the number of missing parts.

Two user-defined thresholds t_1 and t_2 must be specified in the fracture surface extraction algorithm. The appropriate value of the tolerance threshold t_1 is dependent on the quality of the point normals of the underlying fragment mesh. Smaller threshold values (e.g. $t_1 = \pi/8.0$) can be used in case of image data with high spatial resolution and low noise. Contrary, the acceptance margin must be increased to detect the fracture surface in sparsely sampled data or in the presence of noise. Therefore, a value of $t_1 = \pi/6.0$ was required to extract the fracture surfaces from the tested clinical data due to the limited in-plane resolution. However, a wider range typically results in a higher rate of false positives which must be removed in a post-processing step. The automatic removal of false positive detections by applying global clustering will be addressed by future work. The second threshold t_2 corresponds to the local variation of the point normals $\mathbf{n}_k$ with respect to the current normal $\mathbf{n}_j$. All $\mathbf{n}_k$, $\measuredangle(\mathbf{n}_j, \mathbf{n}_k) < t_2$ are assumed to belong to the same cluster as $\mathbf{n}_j$. Based on this assumption, Eq. (4) determines whether $\mathbf{n}_j$ is part of the fracture surface. Therefore, t_2 should be set to the typical angular variation of the normals within a small region of the fracture surface. Best results were achieved with $t_2 = 30-45°$. While smaller t_2-values resulted in gaps in the extracted area, an increase of t_2 caused the region to extend beyond the correct fracture surface.

The final reconstruction described in Section 4.2 relies on user-defined values as well. First, the adjacency between pieces is determined by a distance threshold of 4 mm. The results of the evaluation indicate that the contralateral matching error is sufficiently small (i.e. 2.7 ± 0.9 mm) to generate an adjacency list in this way. As previously mentioned, user-controlled correction of the adjacency information was required in case of multiple overlapping fragments. However, this task can be carried out easily by inspection of the contralateral assembly. Based on the adjacency information, the pairwise registration is initialized by estimating the overlap region of corresponding fracture surfaces. Due to the robust registration method, these regions can be defined roughly using a global threshold. The influence of outliers is reduced iteratively, by updating the overlapping region during optimization. Finally, the kernel correlation-based registration requires to specify the kernel scaling $\bar{\sigma}$, used to smooth out local minima in the cost function of the optimization. Although the optimal value of $\bar{\sigma}$ is dependent on the amount outliers, the registration appears to be robust within a large range of scales (Tsin and Kanade, 2004).

7. Conclusion

In this paper we have presented a method for computer assisted bone reconstruction for complex proximal humerus fractures. User interaction was minimized resulting in short planning times. We have demonstrated that planning based on the contralateral bone is an effective approach for this type of injury. Our matching algorithm allows highly accurate and efficient fragment alignment due to the proposed sampling strategy in conjunction with GPU-based registration. The contralateral matching enabled us to obtain corresponding fragment regions which is a difficult task if performed manually.

However, contralateral matching is not trivial in case of the proximal humerus head and errors in the range of several millimeters were observed even in case of small contralateral differences in anatomy. Therefore, the refinement method based on fracture surfaces was introduced. Pairwise correspondence were obtained by including an additional robust registration step after contralateral matching. Based on the pairwise registration, multi-piece alignment was applied in order to evenly distribute the registration error among all fragments.

The method was evaluated via cadaver experiments and first clinical cases, demonstrating that our computer assisted planning system might be the basis for intraoperative CAS systems for this challenging type of fracture. A clinical study, which is planned in the near future, will be necessary to investigate if the proposed method will lead to quantitative improvement in the surgical outcome.

Acknowledgements

Appendix A

A.1. GPU-based ICP Implementation

The basic ICP approach requires to find closest point pairs between the mesh to be registered (i.e. source mesh) and the target mesh. This is the most expensive part of the algorithm. For acceleration, a parallelization of the closest point queries can be implemented on the GPU. To this end we adapted the idea of Fitzgibbon (2003) to use a distance map for closest point queries. In our approach we generate a uniform grid with a resolution of 1 mm covering the target mesh. The grid is enlarged by a tolerance margin of 10 mm to allow more distant point queries. Each grid cell, covering points of the target mesh, is defined as a surface cell and stores the indices of the points within the cell. Similar to a distance map, all other cells store the index to the nearest surface cell. The data structure is precalculated on the CPU and efficiently encoded in an integer texture on the GPU according to Fig. 13. In a closest point query, the nearest surface cell is determined and the exact distance between query point and stored mesh points is evaluated by testing the distance to all stored points in the cell. For outlier
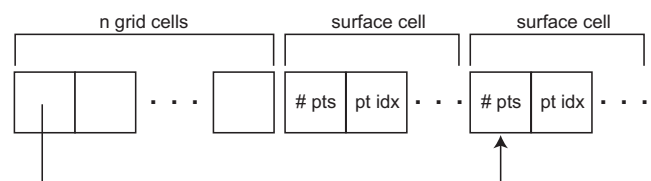

Fig. 13. Data structure for closest point queries encoded in an integer texture.

rejection (Rusinkiewicz and Levoy, 2001), a distance threshold of $\mu + 2\sigma$ was used in each ICP iteration where μ is the average distance of the point-pairs and σ the standard deviation, respectively. The least-squares minimization is another part of the ICP algorithm that can be parallelized and executed on the GPU to gain more efficiency. In our implementation we minimize the point-plane error metric proposed by Chen and Medioni (1992). This requires to solve the linear system $C \cdot x = b$ where C is a symmetric 6×6 matrix, x the vector of transformation parameters, and b is the residual vector (Gelfand et al., 2003). Since each point pair independently contributes to the elements of C and b, the parallel reduction sum algorithm of Harris et al. (2007) can be used in the GPU implementation. The overall GPU-based ICP implementation can be outlined as follows:

Algorithm 2. GPU-based ICP registration

Require: upload source points, target points, target normals, distance query map to GPU.
  allocate array closest_pts[# source points]
  $i \leftarrow 0$ {ICP iteration}
  $T_i \leftarrow identity$ {4×4 transformation matrix of source mesh}
  repeat
    allocate $\mu \leftarrow 0$, $\sigma \leftarrow 0$ in shared memory
    for every source point **in parallel do**
      closest_pts[threadId] $\leftarrow$ do closest point query for $T_i \cdot$ source_pts[threadId],
      update μ, σ using sum reduction algorithm in shared memory
    end for
    allocate shared memory for $C = c_1 \ldots c_{21}$ and $b = b_1 \ldots b_6$ {C is symmetric}
    for every source point **in parallel do**
      $s \leftarrow T_i \cdot$ source_pts[threadId]
      $t \leftarrow$ target_pts[closest_pts[threadId]]
      if $\|s - t\| < \mu + 2\sigma$ **then**
        update b and C using sum reduction algorithm in shared memory
      end if
    end for
    download C and b to CPU
    $T_{i+1} \leftarrow$ solve $C \cdot x = b$ on CPU
    $i \leftarrow i + 1$
  until convergence

References

Beliakov, G., Ugon, J., 2007. Implementation of novel methods of global and nonsmooth optimization: GANSO programming library. Optimization 56 (5–6), 543–546. ISSN: 0233-1934.

Bicknell, R.T., Delude, J.A., Kedgley, A.E., Ferreira, L.M., Dunning, C.E., King, G.J., Faber, K.J., Johnson, J.A., Drosdowech, D.S., 2007. Early experience with computer-assisted shoulder hemiarthroplasty for fractures of the proximal humerus: development of a novel technique and an in vitro comparison with traditional methods. Journal of Shoulder and Elbow Surgery 16 (3), 117–125.

Chen, Y., Medioni, G., 1992. Object modelling by registration of multiple range images. Image and Vision Computing 10 (3), 145–155.

Chetverikov, D., Svirko, D., Stepanov, D., Krsek, P., 2002. The trimmed iterative closest point algorithm. In: International Conference on Pattern Recognition, pp. 545–548.

Delude, J.A., Bicknell, R.T., Mackenzie, G.A., Ferreira, L.M., Dunning, C.E., King, G.J., Johnson, J.A., Drosdowech, D.S., 2007. An anthropometric study of the bilateral anatomy of the humerus. Journal of Shoulder and Elbow Surgery 16 (4), 477–483.

Descoteaux, M., Audette, M., Chinzei, K., Siddiqi, K., 2006. Bone enhancement filtering: application to sinus bone segmentation and simulation of pituitary gland surgery. Computer Aided Surgery 11, 247–255.

Douros, I., Buxton, B., 2002. Three-dimensional surface curvature estimation using quadric surface patches. In: Scanning 2002 Proceedings.

Fitzgibbon, A.W., 2003. Robust registration of 2D and 3D point sets. Image and Vision Computing 21 (13–14), 1145–1153.

Fitzpatrick, J., West, J., Maurer, J.C.R., 1998. Predicting error in rigid-body point-based registration, medical imaging. IEEE Transactions on 17 (5), 694–702.

Gelfand, N., Ikemoto, L., Rusinkiewicz, S., Levoy, M., 2003. Geometrically stable sampling for the ICP algorithm. In: 3-D Digital Imaging and Modeling, pp. 260–267.

Gerber, C., Werner, C.M.L., Vienne, P., 2004. Internal fixation of complex fractures of the proximal humerus. Journal of Bone and Joint Surgery 86 (6), 848–855. British volume.

Harders, M., Barlit, A., Gerber, C., Hodler, J., Székely, G., 2007. An optimized surgical planning environment for complex proximal humerus fractures. In: MICCAI Workshop on Interaction in Medical Image Analysis and Visualization.

Harris, M., Sengupta, S., Owens, J.D., 2007. Parallel prefix sum (scan) with CUDA. In: Nguyen, H. (Ed.), GPU Gems 3, Addison Wesley (Chapter 31).

Horn, B.K., 1987. Closed-form solution of absolute orientation using unit quaternions. Journal of the Optical Society of America A 4, 629–642.

Jaramaz, B., Hafez, M.A., Digioia, A.M., 2006. Computer-assisted orthopaedic surgery. Proceedings of the IEEE 94 (9), 1689–1695.

Johnson, A.E., Hebert, M., 1999. Using spin images for efficient object recognition in cluttered 3D scenes. IEEE Transactions on Pattern Analysis and Machine Intelligenc 21 (5), 433–449.

Joskowicz, L., Milgrom, C., Simkin, A., Tockus, L., Yaniv, Z., 1999. FRACAS: a system for computer-aided image-guided long bone fracture surgery. Computer-Aided Surgery 3 (6), 271–288.

Kolmogorov, V., Zabih, R., 2004. What energy functions can be minimized via graph cuts? IEEE PAMI 26, 147–159.

Kontakis, G., Koutras, C., Tosounidis, T., Giannoudis, P., 2008. Early management of proximal humeral fractures with hemiarthroplasty: a SYSTEMATIC REVIEW. Journal of Bone and Joint Surgery – British Volume (11), 1407–1413.

Lindstrom, P., 2000. Out-of-core simplification of large polygonal models. In: SIGGRAPH '00: Proceedings of the 27th Annual Conference on Computer Graphics and Interactive Techniques. ACM Press/Addison-Wesley Publishing Co., New York, NY, USA, pp. 259–262.

Lorensen, W.E., Cline, H.E., 1987. Marching cubes: a high resolution 3D surface construction algorithm. In: SIGGRAPH '87: Proceedings of the 14th Annual Conference on Computer Graphics and Interactive Techniques, vol. 21. ACM Press, pp. 163–169.

Masuda, T., Sakaue, K., Yokoya, N., 1996. Registration and integration of multiple range images for 3-D model construction. in: ICPR '96: Proceedings of the 1996 International Conference on Pattern Recognition (ICPR '96), vol. I. IEEE Computer Society, Washington, DC, USA, pp. 879–883.

Mederos, B., Amenta, N., Velho, L., de Figueiredo, L.H., 2005. Surface reconstruction from noisy point clouds. In: SGP '05: Proceedings of the Third Eurographics Symposium on Geometry Processing. Eurographics Association, Aire-la-Ville, Switzerland, Switzerland, pp. 53–72.

Moghari, M.H., Abolmaesumi, P., 2008. Global registration of multiple bone fragments using statistical atlas models: feasibility experiments. In: Engineering in Medicine and Biology Society, 2008. EMBS 2008. 30th Annual International Conference of the IEEE, pp. 5374–5377.

Mount, D., Arya, S., 1997. ANN: a library for approximate nearest neighbor searching. In: Proceedings of the 2nd CGC Workshop on Computational Geometry.

Nakajima, Y., Tashiro, T., Okada, T., Sato, Y., Sugano, N., Saito, M., Yonenobu, K., Yoshikawa, H., Ochi, T., Tamura, S., 2004. Computer-assisted fracture reduction of proximal femur using preoperative CT data and intraoperative fluoroscopic images. International Congress Series 1268, 620–625. cARS 2004 – Computer Assisted Radiology and Surgery. Proceedings of the 18th International Congress and Exhibition.

Naranja, J.R., Iannotti, J.P., 2000. Displaced three- and four-part proximal humerus fractures: evaluation and management. Journal of American Academy of Orthopaedic Surgeons 8 (6), 373–382.

Neer, C.S., 1970. Displaced proximal humeral fractures: Part I. Classification and evaluation. Journal of Bone Joint Surgery – American volume 52 (6), 1077–1089.

Neer, C., 2002. Four-segment classification of proximal humeral fractures: purpose and reliable use. Journal of Shoulder and Elbow Surgery 11 (4), 389–400.

Okada, T., Iwasaki, Y., Koyama, T., Sugano, N., Chen, Y.-W., Yonenobu, K., Sato, Y., 2009. Computer-assisted preoperative planning for reduction of proximal femoral fracture using 3-D-CT data. Biomedical Engineering, IEEE Transactions on 56 (3), 749–759.

Papaioannou, G., Karabassi, E.-A., 2003. On the automatic assemblage of arbitrary broken solid artefacts. Image and Vision Computing 21 (5), 401–412.

Press, W.H., Teukolsky, S.A., Vetterling, W.T., Flannery, B.P., 2002. Numerical Recipes in C++: The Art of Scientific Computing. Cambridge University Press. ISBN: 0521750334.

Pulli, K., 1999. Multiview registration for large data sets. In: 3-D Digital Imaging and Modeling, 1999. Proceedings. Second International Conference on, pp. 160–168.

Reineck, J., Krishnan, S., Burkhead, W., 2007. Four-part proximal humerus fractures: evaluation and treatment. Hand Clinics 23 (4), 415–424.

Rodrigues, M., Fisher, R., Liu, Y., 2002. Special issue on registration and fusion of range images. Computer Vision and Image Understanding 87 (1–3), 1–7. ISSN: 1077-3142.

Ron, O., Joskowicz, L., Milgrom, C., Simkin, A., 2003. Computer-based periaxial rotation measurement for aligning fractured femur fragments from CT: a feasibility study. Computer Aided Surgery 7 (6), 332–341.

Rusinkiewicz, S., Levoy, M., 2001. Efficient variants of the ICP algorithm. In: 3-D Digital Imaging and Modeling, 2001. Proceedings. Third International Conference on, pp. 145–152.

Schneider, P.J., Eberly, D.H., 2002. Geometric tools for computer graphics. Morgan Kaufmann.

Schroeder, W., Martin, K.L.B., 2004. The Visualization Toolkit, third ed. Kitware Inc.

Schroeder, W.J., Zarge, J.A., Lorensen, W.E., 1992. Decimation of triangle meshes. In: SIGGRAPH '92: Proceedings of the 19th Annual Conference on Computer Graphics and Interactive Techniques, ACM, pp. 65–70.

Schroeder, W.J., Lorensen, W.E., Linthicum, S., 1994. Implicit modeling of swept surfaces and volumes. In: VIS '94: Proceedings of the Conference on Visualization '94. IEEE Computer Society Press, Los Alamitos, CA, USA, pp. 40–45.

Sharp, G.C., Lee, S.W., Wehe, D.K., 2002. ICP registration using invariant features, pattern analysis and machine intelligence. IEEE Transactions on 24 (1), 90–102.

Shrader, W.M., Sanchez-Sotelo, J., Sperling, J.W., Rowland, C.M., Cofield, R.H., 2005. Understanding proximal humerus fractures: Image analysis, classification, and treatment. Journal of Shoulder and Elbow Surgery 14 (5), 497–505.

Tsin, Y., Kanade, T., 2004. A correlation-based approach to robust point set registration. In: ECCV, vol. 3. pp. 558–569.

Westphal, R., Winkelbach, S., Wahl, F., Gosling, T., Oszwald, M., Hufner, T., Krettek, C., 2009. Robot assisted long bone fracture reduction. The International Journal of Robotics Research 28 (10), 1259–1278.

Wijgman, A.J., Roolker, W., Patt, T.W., Raaymakers, Marti, R.K., 2002. Open reduction and internal fixation of three and four-part fractures of the proximal part of the humerus. Journal of Bone and Joint Surgery – American Volume 84 (11), 1919–1925.

Willis, A., Anderson, D., Thomas, T., Brown, T., Marsh, J.L., 2007. 3D reconstruction of highly fragmented bone fractures. in: SPIE Proc. vol. 6512.

Winkelbach, S., Westphal, R., Goesling, T., 2003. Pose estimation of cylindrical fragments for semi-automatic bone fracture reduction. Pattern Recognition 2781, 566–573.

Winkelbach, S., Rilk, M., Schönfelder, C., Wahl, F., 2004. Fast random sample matching of 3d fragments. Pattern Recognition 3175, 129–136.

Zhou, B., Willis, A., Sui, Y., Anderson, D., Brown, T., Thomas, T.P., 2009. Virtual 3D bone fracture reconstruction via inter-fragmentary surface alignment. In: IEEE Workshop on 3D Digital Imaging and Modeling (3DIM). IEEE Computer Society.